

# Low-Redshift $z < 0.2$ Quasars: QSO and Host Galaxy Relationship

Diego Enrique Garcia,<sup>1</sup>[\\*](#) Mark Lacy,<sup>2</sup> Susan Ridgway<sup>2,3</sup>

<sup>1</sup>Middlebury College, 14 Old Chapel Rd., Middlebury, VT 05753, United States

<sup>2</sup>National Radio Astronomy Observatory, 1180 Boxwood Estate Rd, Charlottesville, VA 22903, United States

<sup>3</sup>National Optical Astronomy Observatory, 950 N Cherry Ave, Tucson, AZ 85719, United States

Accepted 2020. Received 2020; in original form 2020

## ABSTRACT

Quasars are among the most energetic phenomena in the universe, but their origins remain elusive. Are quasars the result of external gravitational interactions or are they instead the result of processes that occur within the host galaxy itself? To answer our question, we analyze a sample of 357 quasi-stellar objects (QSOs) which were selected by matching two million objects from the first epoch of the VLA Sky Survey (VLASS) with the *Gaia* DR2 catalog, removing those objects with high proper motion, and restricting our search to objects with optical magnitude  $g < 17$  and with  $z < 0.2$ . Out of our 357 quasar sources, 342 had optical galaxy images that we could analyze. The narrow redshift range allowed us to observe quasars that live in the same epoch and the low redshift of our sample allowed us to more easily see optical features in the host galaxies. We qualitatively and quantitatively classified our quasar images to detect different galaxy morphologies that may give clues about gravitational interactions occurring in each host galaxy. We visually classified the presence of extended emission, the galaxy type of our host galaxy, as well as noted the presence of close companions or mergers. We found that 77% of our sources were hosted by elliptical galaxies, 18% were hosted by spiral galaxies, and 5% by galaxies demonstrating tidal tail features. To objectively characterize our hosts, we calculated the rotational asymmetry, the Gini Coefficient, and the Second Order Moment of Brightness ( $M_{20}$ ) for our 342 quasars, and did a Principal Component Analysis to find the most significant relationship when plotted against luminosity and found that while the Asymmetry and  $M_{20}$  had only a minor correlation with luminosity, higher Gini Values correlated with smaller values in both optical and radio luminosity and in their luminosity ratio (radio/optical).

**Key words:** black hole physics – accretion

## 1 INTRODUCTION

Quasars are among the most powerful and energetic objects in the universe, and they offer cosmologists a glimpse into universe's earliest days. Almost all galaxies are thought to host Super Massive Black Holes (SMBH) in their central regions. While most galaxies are quiescent, some SMBH accrete material (such as gas or stars) that fall within the central region of the host galaxy where the quasar's accretion disk is located. However, the genesis of these Active Galactic Nuclei (AGN) remains contentious. Certain mysteries abound, the most significant of which being the origin of the material that fuels AGN activity (Schmitt 2001). Quasars that live in spiral galaxies, which have abundant reservoirs of gas, can receive this accretion material from their host unlike those sources contained in elliptical galaxies, where the prevalence of gas is minimal.

Even if we assume that the material that causes this accretion originates from the quasar's host galaxy, what are the forces that cause this mass to lose angular momentum and fall inwards towards

the SMBH? As Letawe et al. (2010) mentions, one favored explanation for the QSO phenomenon is that successive gravitational interactions or galactic mergers disturb the structure of the host, which would allow for material to be brought closer to the central regions where the accretion disk is located and possibly trigger activity. Some studies, such as Schmitt et al. (2001), disagree with this interpretation, citing that the percentage of mergers in active galaxies are not any higher than the percentage of mergers in non-active galaxies. These studies, however, do not consider subtle indicators of intergalactic gravitational interaction that could draw mass deposits towards the central regions of a host galaxy. Indicators such as faint tidal tails and close companions can easily be missed in shallow images. It is also important to use quantitative parameters describing lumpiness, concentration, or asymmetry to objectively characterize compact morphological features to describe the structure of each host galaxy.

As such, studying the relationship between a quasar and the galaxy it lives in is paramount to understanding if quasars are the result of external gravitational interactions, or if they are instead the result of processes that occur within the host galaxy itself. To study

\* E-mail: dgarcia@middlebury.edu

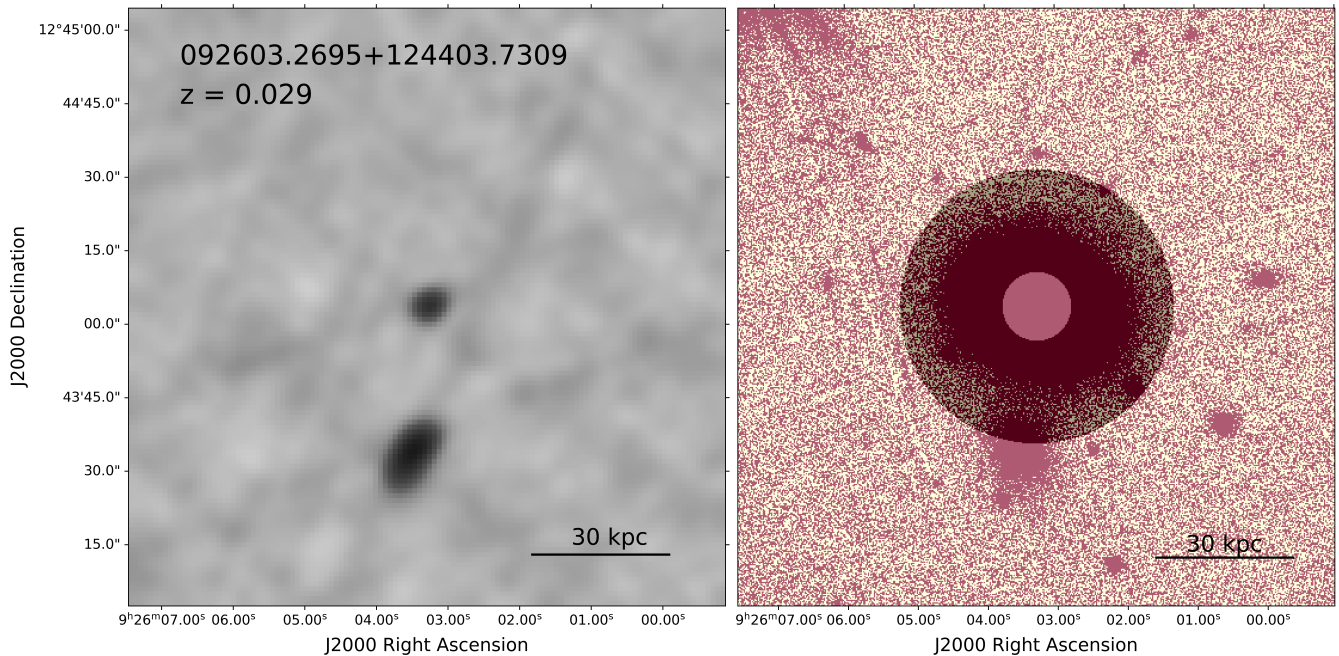


**Figure 1.** Images of galaxy UGC5025. *Left.* Radio VLASS image smoothed with a Gaussian filter showing possible radio emission jet from quasar. *Right.* Optical PanSTARRS r-band image of galaxy, detailing the presence of a close companion to the galaxy. The galactic coordinates and redshift of our source are located on the upper left. UGC5025 is a particularly interesting quasar source as it may be a dual-AGN system. The VLASS image contains what might have been extended radio emission at RA: 3.5s,  $\delta$ : 30.0', but because there is optical overlap with a close companion in this same region in the PanSTARRS image, it is not classified as extended radio emission. As such, this second source may well be a dual-AGN system, though confirming this will require further research.

this relationship, we study a sample of 357 bright quasars sources at both radio and optical wavelengths, obtained by matching objects in the VLA Sky Survey with the Gaia astrometric survey. In Section 2, we will discuss the construction of the sample and the observations. In Section 3, we discuss the methods in which we quantitatively and qualitatively describe the host galaxies and radio emission from our quasars, including quasar and host galaxy separation as well as the methods in which we reduce and interpret our data. Section 4 discusses the results and correlations of our investigation along with subsequent discussion of our findings, and we present our conclusions in Section 5.

## 2 SAMPLE AND OBSERVATIONS

### 2.1 Sample

We used a new survey of bright (optical magnitudes  $g < 17$ ) quasars based on detections in the VLA Sky Survey (VLASS). VLASS is designed to complement the optical imaging surveys of SDSS, PanSTARRS, and the Legacy Survey of Space and Time (LSST), by offering a view of the radio sky at comparable resolution to the optical surveys. By restricting our survey to optical magnitudes  $g < 17$ , we focus on the bright quasar population containing luminous AGN and quasars at low redshifts, where our sources can be studied in detail. For this project, we focus on ( $z < 0.2$ ) quasar hosts. Limiting our scope to nearby sources will allow us to detect faint galaxy features in both the optical and radio that may be lost at higher redshifts because of surface brightness dimming, and looking at a narrow range of redshifts allows us to examine sources in the same epoch.

In order to produce a list of candidate quasars with minimum contamination by radio-bright stars and quiescent galaxies, two mil-

lion objects from the first epoch of all-sky imaging with VLASS were matched to the *Gaia* DR2 catalog within a  $1.^{\prime\prime}5$  search radius. We found 148,000 sources in common. Because quasars lack significant proper motion, further selection criteria eliminated objects with proper motion/uncertainty  $> 3$  (corresponding to  $\gtrsim 1$  mas/yr) which removes most radio-bright stars. Optical color criteria was not used as a selection criteria in order to pick up AGN with unusual colors (for example, quasars reddened by dust in either their host galaxy, in the IGM, or, if they are situated near the Galactic plane, by the Milky Way). Our selection process gave us a sample of 357 quasar sources, of which we were able to obtain *r*-band optical images for 342 of them (the remaining 15 sources were outside the coverage of our optical surveys, the NOAO Legacy Survey and PanSTARRS). Because we created our sample by starting with VLASS detections, we have VLASS radio images of all 357 sources.

### 2.2 Observation

Our radio images were collected from VLASS, which images the entire sky north of declination  $\delta > -40^{\circ}$  at 2-4 GHz and  $2.5''$  resolution, with observations carried out in three epochs. The RMS sensitivity is  $120 \mu\text{Jy}/\text{beam}$  at a mean frequency of 3 GHz (Lacy et al. (2020)). Our optical data were taken from two surveys, Data Release 8 (DR8) of the NOAO Legacy Survey (Dey et al. (2019)), which covers  $14,000 \text{ deg}^2$  of sky between  $-18^{\circ} < \delta < +84^{\circ}$ ; and the DR1 of the Panoramic Survey Telescope and Rapid Response System 1 (Pan-STARRS1) developed by the University of Hawaii's Institute for Astronomy (Chambers et al. (2016)).

The PanSTARRS1 survey used a 1.8 meter telescope and its 1.4 Gigapixel camera situated at Haleakala Observatory to image the sky in five broadband filters ( $g, r, i, z, y$ ). The Legacy Survey is a combination of the DECam Legacy Survey (DECaLS) using

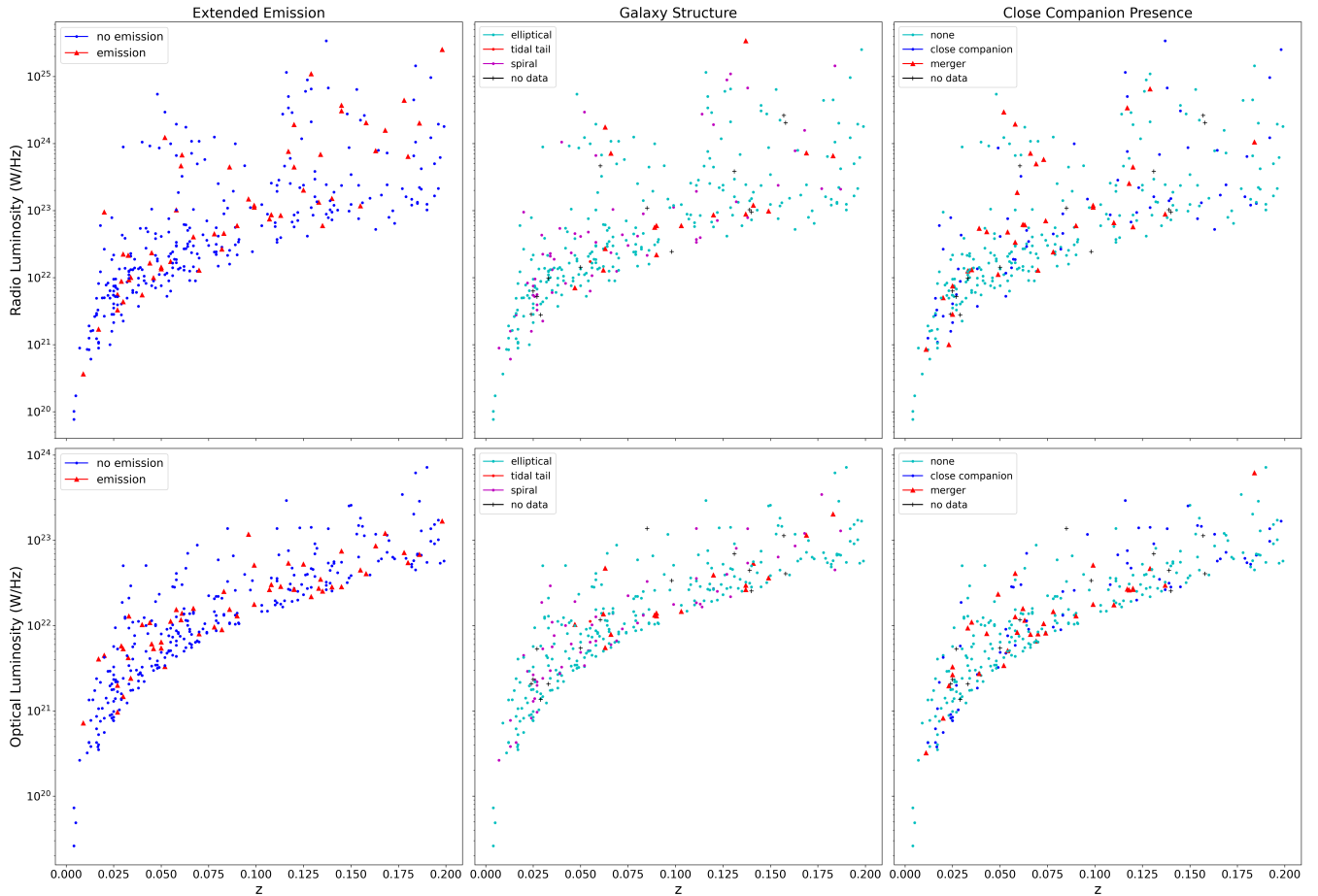


**Figure 2.** Redshift vs. Luminosity plots, with Radio Luminosity on the top row and Optical Luminosity on the bottom row. We plot our three visual inspection classifications in each column. The logarithmic curve present in these plots is the direct result of our  $g < 17$  magnitude limit, as we would not be able to see the faintest stars as we go farther away.

the Blanco 4m telescope located at the Cerro Tololo Inter-American Observatory, Chile; the Mayall z-band Legacy Survey (MzLS) using the MOSAIC instrument on the Mayall 4m telescope at the Kitt Peak Observatory; and the Beijing-Arizona Sky Survey (BASS) using the 90Prime instrument at the Steward Observatory Bok telescope. When choosing which optical images to use for a particular source, we defaulted to images taken by the Legacy Survey because of its greater depth. If no image was present for the source in the Legacy Survey, we used the corresponding image from the PanSTARRS1 survey. The redshifts of our sources were obtained either from the literature, or with the Kast spectrograph on the Shane 3m telescope at Lick Observatory, with the 600/4310 (number 2) grism in the blue spectrum and the d57 dichroic and the 600/7500 (number 2) grating in the red spectrum in order to give continuous coverage from 3500–8500 Å. 2x8 minutes of integration time was used. Throughout this paper, we adopt the following cosmological parameters:  $H_0 = 70 \text{ km s}^{-1} \text{ Mpc}^{-1}$ ,  $\Omega_m = 0.30$ , and  $\Omega_\lambda = 0.70$ .

### 3 METHODS AND IMAGE ANALYSIS

We visually inspect our radio and optical images, searching for extended radio emission in the form of jets, as well as for the presence of gravitational interactions in the host galaxies of our sources, particularly features that indicate mergers or close companion inter-

actions such as faint tidal tails. Using non-parametric values (that require no a priori knowledge of our hosts or model fits), we can understand the structural composition of our host galaxy sample. In order to eliminate redundancy in our parameters, we do a Principal Component Analysis to analyze our data. Section 3.1 below describes the methods of visual inspection we used when categorizing our sample. In Section 3.2, we describe the parameters we used to describe our galaxy structures, and we describe the methods of our Principal Component Analysis in Section 3.3.

#### 3.1 Visual Inspection of Radio Emission and Galaxy Morphology

We visually inspected the radio and optical images of our sample of 357 quasar sources. All 359 radio images came from VLASS, while 220 optical images came from NOAO, and 121 optical images came from PanSTARRS. The remaining 15 sources have coordinates out of range for both surveys and as a result we have no optical data for them. Through visual inspection, we characterized our radio images by presence of extended radio emission (interaction of synchrotron radiation jets from the quasar interacting with either the ISM or the IGM), and our optical images according to the host galaxy structure, and the presence of close companions or mergers. To classify our images by presence of extended radio emission, we used both the VLASS radio images and the corresponding Legacy or

PanSTARRs1 optical image of each respective source. Our criteria for possible extended emission required that the source show radio emission less than 2.5 arcminutes away (Kužmicz et al. (2018)), that there is no optical emission that overlaps with the radio emission we have (as we would not detect synchrotron radiation at optical wavelengths and overlap may suggest the presence of a separate nearby quasar source), and some evidence of backflow, with a tail from the emission pointing back towards the quasar nucleus. The presence of backflow becomes increasingly important as the emission gets farther away from the source. For some sources with VLASS images featuring ambiguous radio emission, we also consulted image data from the NRAO VLA Sky Survey (NVSS; ?) to corroborate our findings. To categorize our survey sample by host galaxy structures, we visually classified each galaxy as either elliptical, spiral, or a tidal tail. Galaxies with irregular morphologies would most likely have been categorized as either a spiral or tidal tail galaxy, depending on which of that galaxy's features were most prominent. We also classified the presence of close companions or mergers with the galaxy. To be classified as a close companion, a nearby galaxy must have been less than a host galaxy radius away from the edge of the source, and of comparable size to the host galaxy to be categorized as such. To be classified as a merger, the neighboring galaxy must be touching and involved with the host galaxy. When categorizing the galaxy structure of host galaxies that have mergers, we focus only on the structure of the host galaxy.

### 3.2 Non-Parametric Quantification of Galaxy Morphology

We use a non-parametric approach designed by Lotz et al. (2004) and Scarlata et al. (2007) that has been widely adopted, and quantify the light distribution of our host galaxies in our optical r-band images. The four parameters we aim to calculate are the Gini Coefficient (G), the second order moment of brightness 20% ( $M_{20}$ ), the Concentration (C), and the Rotational Asymmetry (A). To calculate the values of G,  $M_{20}$ , and C, we needed to separate the quasar light from the light coming from the galaxy host. To do so, we created an annulus mask for our galaxy images, where the inner radius of the annulus is 7.5 kpc across to separate light from the QSO and the host galaxy, and the outer radius is a distance of 30 kpc, which is done to exclude the light from close-companions and other nearby phenomena. For the asymmetry, we did not need to separate the QSO from the galaxy, so we instead only used a circular mask with a 30 kpc radius. To correct for noise, we subtract the median flux pixel value of each image to every pixel in the galaxy image. Below we list a description of each parameter we used to describe our host galaxy structure.

**Gini Coefficient** The Gini Coefficient, or the "lumpiness" of a galaxy image, is a parameter that gives information on how evenly distributed galaxy light is among the pixels in an image. Although it originated in economics as a way to measure a nation's wealth inequality, in astronomy the Gini Coefficient tells us how unequal light is distributed in an image, independent of pixel position. An image where one pixel holds all of the flux would have a value of  $G = 1$ , while an image with flux evenly distributed throughout every pixel would have a Gini value of  $G = 0$ . To calculate the Gini Coefficient, we use the following equation where we first sort  $X_i$ , the list of flux values for each pixel in the mask, into increasing order and use

$$G = \frac{1}{\bar{X}n(n-1)} \sum_i^n (2i - n - 1)X_i \quad (1)$$

where  $\bar{X}$  is the mean pixel value and n is the number of pixels in the mask (Lotz 2004).

**Rotational Asymmetry** One well established way to quantify the presence of mergers in a galaxy system is through the rotational asymmetry, as seen in Letawe et al. (2010), Scarlata et al. (2007), Conselice et al. (2003), and many more. Our asymmetry calculation is done by rotating the image 180° and subtracting the rotated image from the original image. Instead of an annulus mask, we apply a circular mask to the galaxy then sum the residual flux in that region and divide that result by twice the flux of the original region. The correct center of rotation greatly influences the calculated asymmetry for each source. Certain galaxy images may not be centered at the exact center of the galaxy, so to account for this, we find the position that minimizes the asymmetry calculation and use that resulting value. We use:

$$A = \min \left( \frac{\sum |I_o - I_{180}|}{2 \sum |I_o|} \right) \quad (2)$$

where  $I_o$  and  $I_{180}$  are the intensity of a pixel in the initial image and in the image flipped by 180°, respectively. Asymmetry values range from 0 to 1, where values close to 1 have high values of asymmetry and values close to 0 are more radially symmetric.

**Second Order Moment of Brightness 20% ( $M_{20}$ )** The second order moment of brightness 20%, or  $M_{20}$ , is a parameter that quantifies the spatial distribution of the brightest 20% of pixels assigned to our galaxy host. It is best understood as an analog for distribution of Moment of Inertia, where instead of mass, we use pixel brightness. It is a useful metric that describes the distribution of bright nuclei, spiral arms, off-center star clusters, etc. that may be present in a galaxy. To find  $M_{20}$ , we add up the  $M_i$  values of the brightest 20% of pixels and divide that over the total M value of the galaxy,  $M_{tot}$ :

$$M_{tot} = \sum_i^n M_i = \sum_i^n f_i [(x_i - x_c)^2 + (y_i - y_c)^2] \quad (3)$$

where  $x_c$  and  $y_c$  are the position of the galaxy's center. Because the  $M_{tot}$  is dependent on the position of bright features, finding a correct center for each galaxy is important to getting an accurate value, especially if the galaxy's center is initially off-center in our optical image. To find our galaxy center, we find values of  $x_c$  and  $y_c$  that minimize  $M_i$ . To calculate  $M_{20}$ , we order the pixels assigned to the galaxy in descending order and compute a value of  $M_i$  for each flux value until the sum of our brightest pixels is 20% of the total flux. We then divide by  $M_{tot}$  to remove any dependence on galaxy or image size:

$$M_{20} \equiv \log_{10} \left( \sum_i M_i / M_{tot} \right), \text{ while } \sum_i f_i < 0.2f_{tot} \quad (4)$$

where n is the number of pixels we assigned to our host galaxy. All values of  $M_{20}$  are negative. As such  $M_{20}$  values closer to 0 indicate galaxy hosts with concentrated brightness near the center of the galaxy, while values of  $M_{20}$  that are more negative and approach -inf indicate galaxies with brightness concentrations farther away from their galaxy centers. Because  $M_{20}$  is also dependent on location, the values of  $x_c$  and  $y_c$  are those that minimize  $M_{tot}$  for each galaxy.

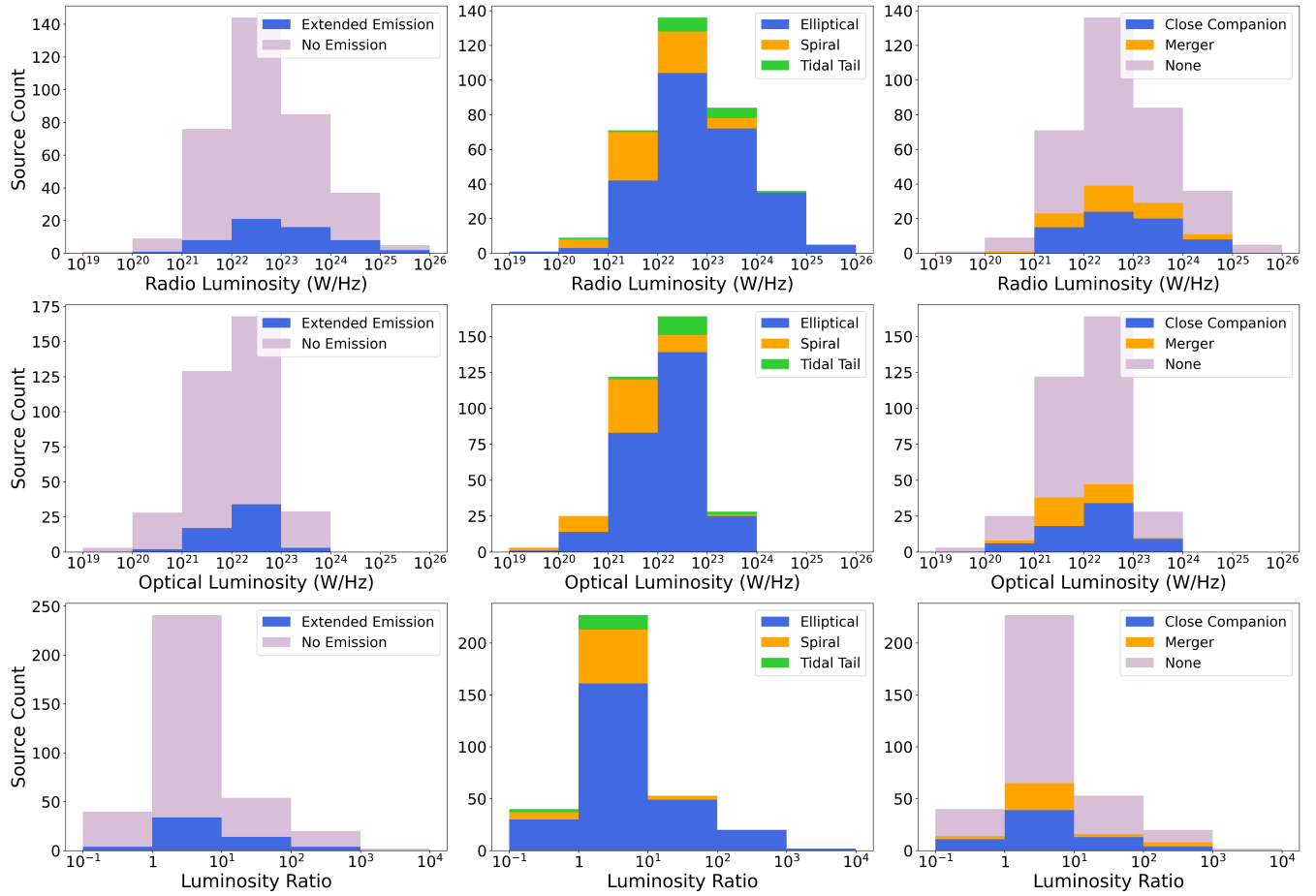


**Figure 3.** Luminosity histograms detailing the composition of our visual inspection classification. The histograms in the top row are plotted against Radio Luminosity, histograms in the middle row are plotted against Optical Luminosity, and the histograms on the bottom row are plotted against the Luminosity Ratio, which is Radio Luminosity/Optical Luminosity. We detail the composition of our three visual inspection classifications in each column: in the left column, we detail how many sources demonstrated extended radio emission in their VLASS images; in the middle column, we highlight the host galaxy type of our sources; and in the right column, we show what number of sources had close companion galaxies or mergers.

**Table 1.** Results of our Visual Inspection Classification. Below we show our findings for the 342 sources we visually classified, divided into presence of close companion galaxies or mergers, presence of extended radio emission, and galaxy structure type. The table below shows the percentage of the total survey for each classifier. The specific number of sources appears in brackets next to percentage.

Galaxy Structure (1)	Visual Inspection Classification					
	Close Companion Presence			Extended Radio Emission		
	Close Companion (2)	Merger (3)	None (4)	Yes (5)	No (6)	Total (7)
Elliptical	17.3 [59]	7.6 [26]	51.6 [177]	12.3 [42]	64.3 [220]	76.6 [262]
Spiral	2.0 [7]	2.0 [7]	14.3 [49]	3.2 [11]	15.2 [52]	18.4 [63]
Tidal Tail	0.3 [1]	0.9 [3]	3.8 [13]	0.3 [1]	4.7 [16]	5.0 [17]
Total	19.6 [67]	10.5 [36]	69.9 [239]	15.8 [54]	84.2 [288]	100.0 [342]

### 3.3 Principal Component Analysis

The galaxy structure parameters we calculated using our optical r-band images are important tools for understanding our host galaxies morphologies, as they provide an objective way to determine the presence of gravitational interactions in each system. While each parameter reveals different information, they still contain a considerable amount of overlap. For instance, there tend to be strong correlations between the  $M_{20}$  and the Gini Coefficient in large sam-

ple sets because of their similar definitions (Lotz 2004). One way to reduce this informational redundancy is to do a Principal Component Analysis (PCA), which reduces the dimensionality of our sample, while minimizing information loss.

In a PCA, we find new variables to act as coefficients (or "weights") for our original parameters, where every new variable independent of each other, so that we can re-write our data as a linear equation of our weights multiplied by our original parameters. Our linear equations are called *Principal Components*, where each  $PC_i$

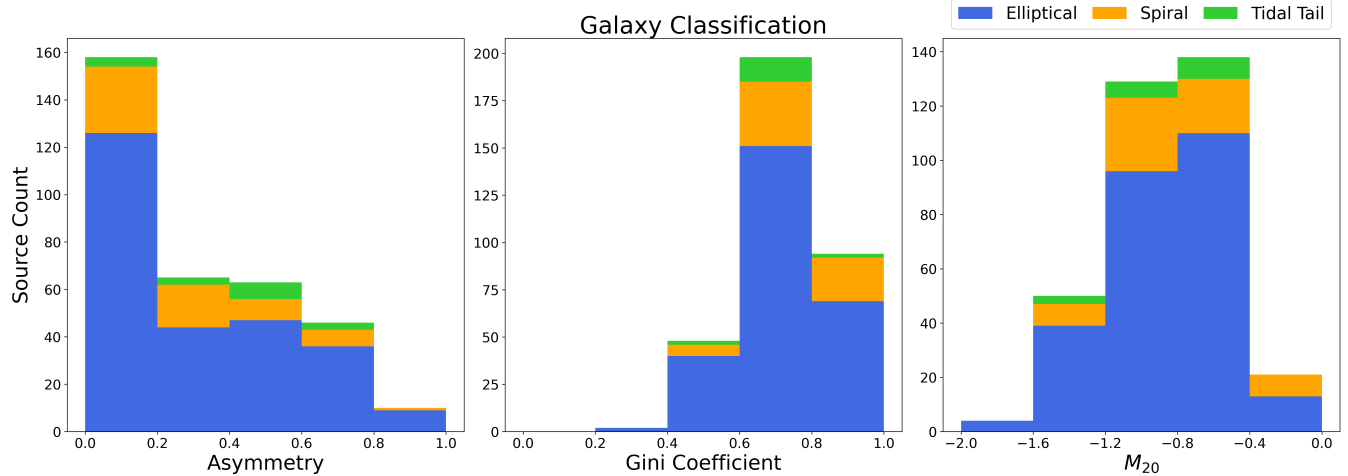


**Figure 4.** Histogram of quantitative parameter distribution with galaxy classification highlighted. From left to right, each plot shows the Asymmetry value, the Gini Coefficient, and the  $M_{20}$  value of each source.

**Table 2.** Results of our Principal Component Analysis. Columns (2) to (4) refer to our three PCs. The first row gives the eigenvalue (i.e., variance) of the data along the direction of the corresponding PC. The second row shows the proportion (the fraction of the variance) and the third row the cumulative proportion of each PC, respectively. The last three rows list the weights assigned to each input  $M_{20}$ , A, and G, in the linear combination of each PC of the form  $PC_i = \alpha \cdot M_{20} + \beta \cdot G + \gamma \cdot A$ , with each coefficient  $\alpha$ ,  $\beta$ , and  $\gamma$  given by the number listed in each column.

Results of ZEST Principal Component Analysis			
Variable (1)	PC <sub>1</sub> (2)	PC <sub>2</sub> (3)	PC <sub>3</sub> (4)
Eigenvalue	1.734	0.690	0.576
Proportion	0.58	0.23	0.19
Cumulative	0.58	0.81	1.00
$M_{20} (= \chi_1)$	0.548	0.582	0.601
Gini ( $= \chi_2$ )	0.816	-0.528	-0.233
Asymmetry ( $= \chi_3$ )	-0.181	-0.618	0.765

(where  $i = 1, \dots, n$  where  $n$  is the number of parameters) is of the format  $PC_i = \alpha \cdot x_1 + \beta \cdot x_2 + \dots + \gamma \cdot x_n$ , where  $x_1$  through  $x_n$  represents the parameter values of a source, and the Greek letters represent the parameter weights for that principal component.

To obtain these variables in our PCA, we create an  $n \times m$  data matrix, where  $m$  is the number of sources we have with optical images of their host galaxy (342 sources). Each parameter value that we calculated for a source is then standardized by subtracting the median value of the respective parameter and dividing the result by the parameter's standard deviation. From here, we get an  $n \times n$  covariance matrix  $S$  from our data matrix, and find the corresponding eigenvectors and eigenvalues of  $S$ . Because  $S \geq 0$  and is symmetric, our resulting eigenvalues will be positive and real. We organize our eigenvalues (and their corresponding eigenvectors) in descending order, which means that our orthogonal bases are aligned in order of decreasing variance. This means that the bases that appear first contain most of the information in our analysis, and each value in the eigenvector contains the weights for that principal component.

## 4 RESULTS

We present the results of our analysis below. The results of our visual inspection are presented first, followed by our quantitative parameters, and then our PCA findings. We try to find correlations between quasar properties and evidence of gravitational influences in their host galaxies.

### 4.1 Host Galaxy Visual Inspection Classifications

In Figure 2, we plotted the redshift values we obtained at the Lick Observatory with our calculated optical and radio luminosity values. The logarithmic curve that can be seen in Fig. 2 is a result of our selection criteria: because of our magnitude limit of  $g < 17$ , we see less bright sources at lower redshifts, and the farther we go out, dimmer sources will be filtered out. In Table 1, we show the results of our visual classification as a percentage of the total number of host galaxies. A detailed table of the specific criteria we assigned for each source can be found in the appendix. Almost 77% of our host galaxies were elliptical, while 18% were spiral, and 5% had tidal tail features. Our results correspond with the predictions of Dunlop et al. (2003), who suggests that at higher radio luminosities, most quasars are hosted by elliptical galaxies. The presence of extended radio emission was uncommon in our sample, as only 54 of our sources (approximately 16%) fit our criteria to be categorized this way. When searching for close companions, 30% of our sources had some sort of neighboring galaxy nearby, with almost 20% of our sources having a close companion galaxy nearby their host galaxy, and 11% showing signs of merger activity. Although tidal tails and mergers are the clearest example of a host galaxy showing evidence of gravitational interaction with an external source, it is noticeable that there is little overlap between these two features: only 0.9% of our total sample had both. As a percentage of total mergers, only 9% came from tidal tail galaxies, and as a percentage of total tidal tail galaxies, 18% came from galaxies that also had mergers. Most quasars who had both close companion galaxies or mergers were hosted by elliptical galaxies. We found that 88% of sources that had a close companion were elliptical, which is well above the 77% total composition we would expect (given its proportion to the total sample). In comparison, elliptical galaxies make up 72% and 75%

of sources with galaxy that have mergers and galaxies without a neighboring galaxy, respectively.

In Figure 3, we present a luminosity histogram that details the composition of our source's visual classification. From our plots, we see how the presence of non-elliptical galaxies is usually higher at lower luminosities (center column). Below  $10^{21}$  W/Hz in radio and optical luminosity (center top and center plot), an average of 60% of sources are either spiral or tidal tail. From  $10^{21}$  W/Hz until  $10^{24}$  W/Hz in radio luminosity, the percent composition of non-elliptical galaxies steadily decreases in each luminosity bucket from approximately 40% to 24% to 15%. In the optical, this range is much narrower from  $10^{21}$  W/Hz to  $10^{23}$  W/Hz, with 32% and 15% in each bucket. For the luminosity ratio histogram (center bottom), the vast majority of non-elliptical galaxies, more than 82%, have a ratio between 0 and 10. 12.5% of these non-elliptical galaxies have luminosity ratios ranging from 0.1 to 1. It is noteworthy that tidal tail galaxies specifically are very constrained in specific luminosity buckets. We note that the majority of tidal tail host galaxies are present between  $10^{23}$  and  $10^{24}$  W/Hz in the radio, and are most present in the optical between  $10^{22}$  and  $10^{23}$  W/Hz. Like most non-elliptical galaxies, tidal tails are also mainly concentrated at luminosity ratios ranging from 1 to 10.

About 30% of our sources had a close companion or evidence of a merger, which means that these sources have the most direct evidence of possible gravitational interaction with an outside source. The total percent of close companions and mergers remained relatively stable at different magnitudes of radio luminosity and were consistent with the 30% we saw before (right column). Between  $10^{21}$  to  $10^{25}$  W/Hz, the total percentage was around 30% of sources at each luminosity magnitude. Individually, close companions and mergers also composed of consistent percentages throughout these radio luminosity buckets compared to their total percentage (20% and 10%, respectively). This is different at optical luminosities, where the percentage of close companions is much higher at higher optical luminosities. Only 15% of our sources showed the presence of extended radio emission (left column). As seen in the left column of Figure 3, there is a higher percentage of extended radio emission at higher radio luminosities, which is the opposite of what is seen when compared to optical luminosities, where most extended emission is within  $10^{21}$  and  $10^{23}$  W/Hz. While the presence of extended radio emission in elliptical and spiral galaxies are relatively consistent compared to their overall makeup, tidal tail host galaxies tend to have lower rates of extended radio emission compared to their total presence (1.9% of extended radio emission is present in tidal tails while tidal tails make up 5% of all host galaxies).

## 4.2 Quantitative Descriptors

We present the result of our quantitative analysis, where we present the Asymmetry value (A), the Gini Coefficient (G), and the Second Order Moment of Brightness ( $M_{20}$ ) for our 342 sources with host galaxy images at optical wavelengths. In order to check for potential bias, we plotted our parameters against their corresponding redshift and found no significant correlation between parameters and redshift. In Figure 4, we present the overall distribution of the parameters we got for our sample of 342 sources with optical images. For our asymmetry value, 46% of our sources had asymmetry values between 0 and 0.2, and 80% of our sample has an asymmetry below 0.6. For our Gini Coefficient, 85% of our sample had a Gini value higher than 0.6. Only our  $M_{20}$  value was relatively evenly distributed, where almost 80% of our sources are between -1.2 and -0.4. When observing the relationship between our parameters and

our galaxy classifications, we notice that there is a greater presence of non-elliptical galaxies. In the stacked asymmetry histogram on the right in Figure 4, the three lowest asymmetry buckets ranging from 0 to 0.6 collectively had an average of 24% of sources with as either spirals or tidal tails, and the highest asymmetry buckets had a collective 19% of sources as non-elliptical galaxy hosts. Tidal tails were mostly present between asymmetry values of 0.4 and 0.6. When looking at our Gini values, we found that non-elliptical galaxies were found at high percentages at the two highest Gini buckets, where 25% of sources between 0.6 and 1.0 were spiral or tidal tail. This means that our non-elliptical galaxies are typically more lumpy and have images that contain brightness concentrated on fewer pixels. Tidal tail sources were mostly found between Gini values of 0.6 and 0.8. For  $M_{20}$ , most non-elliptical galaxies were at lower  $M_{20}$  values, which indicates that tidal tail and spiral features were present in galaxies with brightness farther away from its center.

In Figure 5, we plotted the result of our three parameters plotted against luminosity. We included a line of best fit for each plot, of the form  $y = m$  (parameter) + b, where m is the slope of the line and b is the intercept. Both m and b for the best fit line can be found above each plot. Our Asymmetry values when plotted against radio and optical luminosity individually all show very slight negative correlations (top left and middle left). However, the luminosity ratio plotted against Asymmetry (bottom left) shows almost no correlation. Our best fit line may be biased due to the high number of sources that are concentrated at values A < 0.2, but our plot generally implies little correlation between Asymmetry and Luminosity. When examining our Gini Coefficients (center column), we notice a stronger trend among all three luminosity values that suggests that increasing Gini value correlates with decreasing luminosity. This trend was strongest for G vs. Radio Luminosity (top center) which has a best fit line of slope value  $m = -4.04$ . For G vs. Optical Luminosity (center plot), the trend was also strong, but decreased slightly with  $m = -2.5$ , and when comparing the radio/optical luminosity ratio (bottom center), we also saw a significant negative correlation of  $m = -1.48$ . When examining the Second Order Moment of Brightness (right column), we also see a general decrease in  $M_{20}$  value. Like the Gini Coefficient, we also saw the strongest trend occur when  $M_{20}$  is plotted against radio luminosity (top right), with a slope of  $m = -0.602$ . The negative correlation decreases when plotted against optical luminosity and the luminosity ratio. Overall, there is a stronger negative correlation between parameters and radio or optical luminosity individually then there is between the parameters and the ratio of the luminosities.

## 4.3 PCA Results

We present the results of our Principal Component Analysis on the normalized parameter values in Table 2. Columns (2) - (4) refer to the three Principal Components (PCs) obtained in the analysis. The first row lists the eigenvalue (i.e., the variance) of the data along the direction of the corresponding PC. The second row shows the fraction of the variance that is explained by each PCs, (i.e., the "power" contained in each PC) and the third row lists the cumulative fraction of the variance. In the last three rows, each column lists the weights in the linear combination that gives the direction of the specific PC. Given our results, we will be focusing on the first two PCs as they together contain 81% of the total variance.

In Figure 6, we present the relationship between Luminosity and each PC, with a line of best fit present. The slopes of our best fit lines can be seen above each plot and in Table 3. As seen in Table 2,

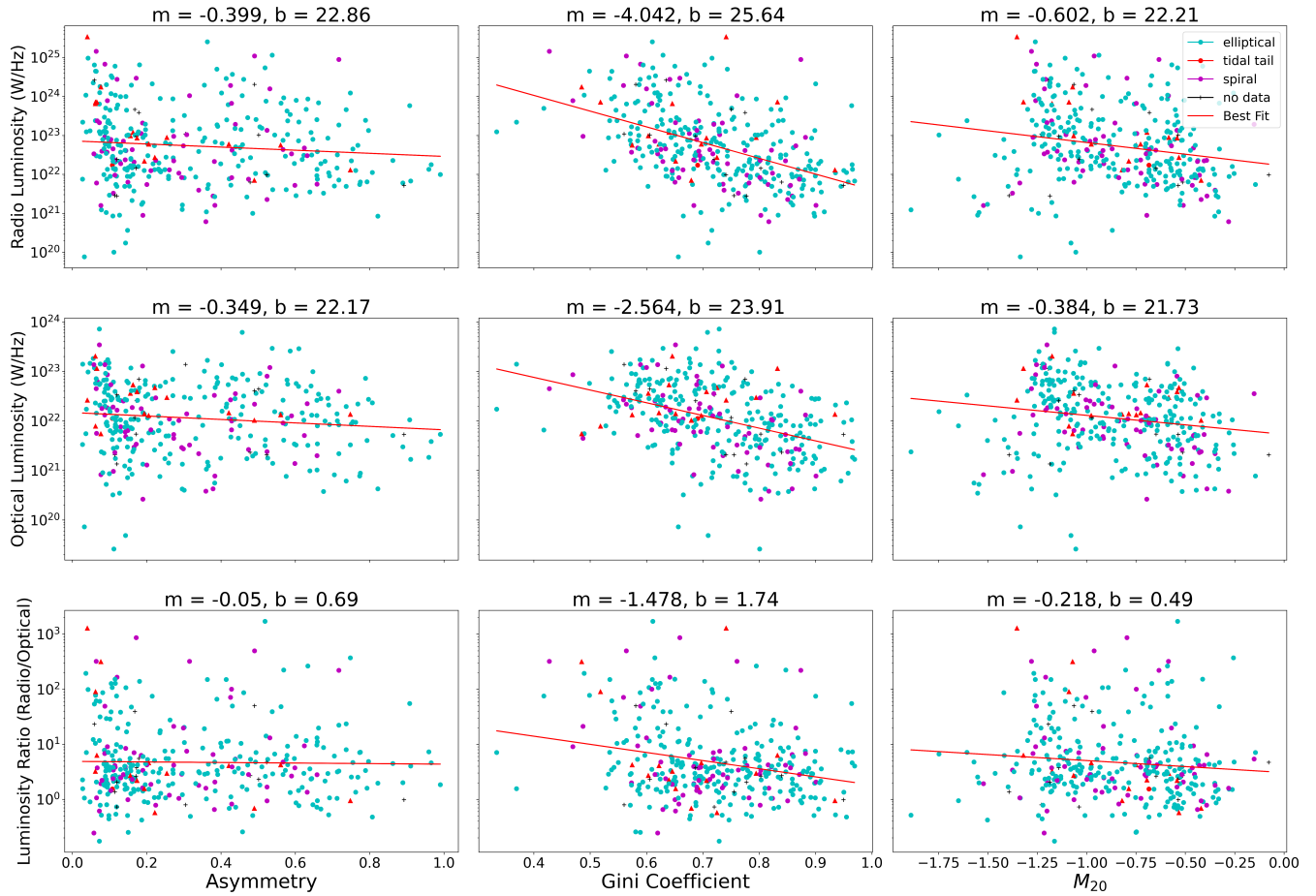


**Figure 5.** Plots showing our Quantitative Parameters vs. Luminosities. Each column from left to right has the Asymmetry value, Gini Coefficient, and the  $M_{20}$  value on the x axis. Plots in the top row have each parameter plotted against the Radio Luminosity, the plots in the middle are plotted against Optical Luminosity, and plots on the bottom row are plotted against the Luminosity Ratio (Radio/Optical). For each plot, we plotted a line of best fit in the form  $y = m$  (parameter) +  $b$ , where the slope and intercept  $m$  and  $b$  are shown above each plot. Each point in the plot is given a distinct color to represent its host galaxy type and the legend can be found on the upper right.

the most significant weight in  $PC_1$  is the Gini Coefficient, which is 0.816. The trend lines for  $PC_1$  (top row) in Figure 6 for both radio and optical luminosity (left and middle columns) have a negative slope. Because the most significant weight is a large positive number and the best fit line decreases with increasing luminosity value, our results suggest that increasing luminosity correlates with a smaller Gini Coefficient, which further corroborates our findings in Section 4.2. In  $PC_2$ , Asymmetry is the largest weight by magnitude and is negative, although in this PC it is important to note that most attributes have similar absolute magnitudes. As such, the important relationship between the different weights is what direction they point in—because the values for the Gini Coefficient and Asymmetry are both negative and only  $M_{20}$  is positive, and because the slope of the best fit line is positive as luminosity increases, higher luminosity values have lower values of Asymmetry and Gini Coefficient. This is a notable, if subtle, result from our Principal Component Analysis, as our analysis in Figure 5 was rather inconclusive about the correlation between the luminosity and asymmetry. This corroborates what we concluded about the Gini Coefficient from the first PC, and implies that more luminous quasars tend to host radially symmetric galaxies. The slopes of the trend lines plotted against the luminosity ratios (right column), both have slopes that are the same sign for their respective PC: the luminosity ratio vs.  $PC_1$  (top

**Table 3.** The result of our PC lines of best fit, as seen in Figure 5. Each row is an equation of Best Fit =  $m$  (parameter)  $x$   $b$ , where  $m$  is the slope,  $b$  is the intercept and  $p$  is the Pearson's correlation coefficient..

P.C. vs. Radio Luminosity			
Subclass	$m$	$b$	$p$
All Radio ( $PC_1$ )	-0.49	11.0	3.38e-19
All Radio ( $PC_2$ )	0.19	-4.7	7.26e-5
All Optical ( $PC_1$ )	-0.58	12.8	2.05e-14
All Optical ( $PC_2$ )	0.26	-6.1	1.0e-4
Ratio ( $PC_1$ )	-0.380	0.208	3.38e-06
Ratio ( $PC_2$ )	0.12	-0.32	9.4e-2

right) has a negative slope and the luminosity ratio vs.  $PC_2$  (bottom right) has a positive slope. Noticeably, neither line of best fit is as steep as the plots where each luminosity was present individually, which fits the general trend (ratio plots also had a smaller slope in our parameter vs. luminosity plot in Figure 5).

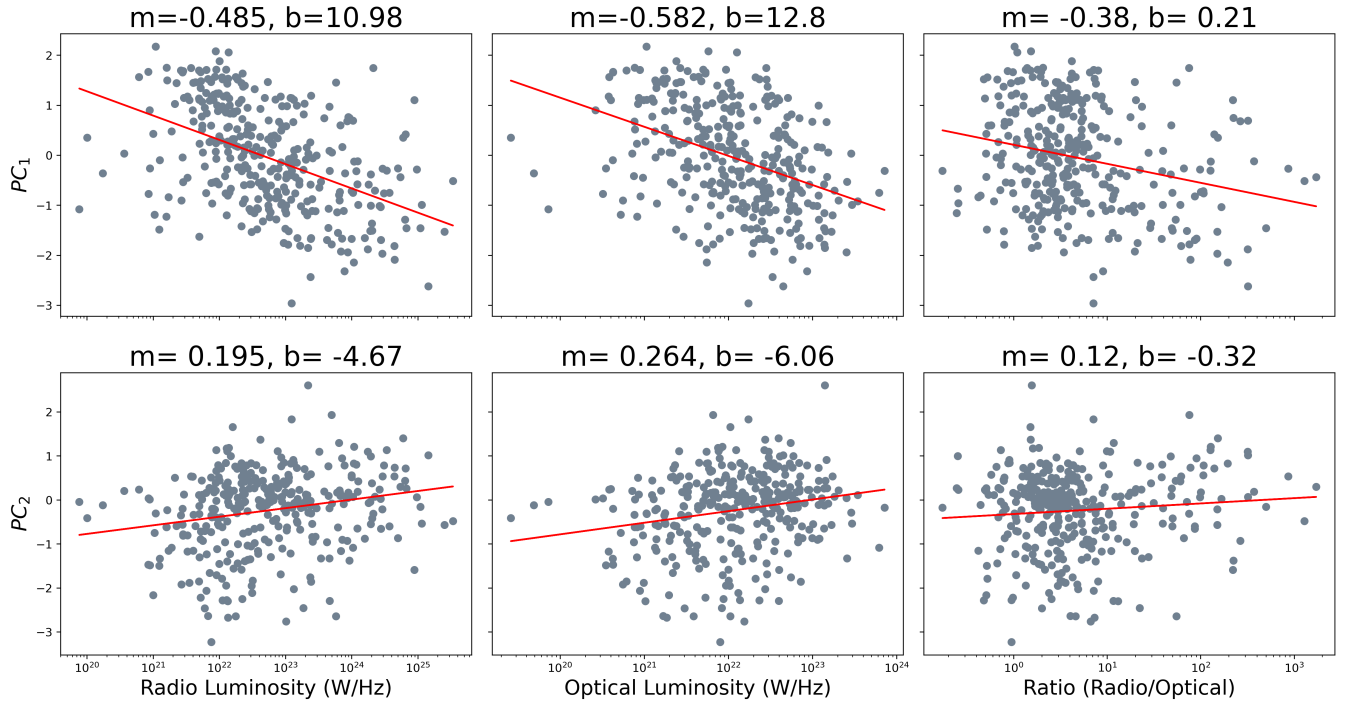


**Figure 6.** Luminosity vs. Principal Component value plots, with line of best fit present. From left to right, each column has the Radio Luminosity, the Optical Luminosity, and the Luminosity Ratio (Radio Luminosity/Optical Luminosity) on the x axis. The top row has each luminosity plotted against the first Principal Component  $PC_1$ , and the bottom row has it plotted against the second Principal Component  $PC_2$ . Each principal component is of the form  $PC_i = \alpha \cdot M_{20} + \beta \cdot G + \gamma \cdot A$ , where  $M_{20}$ ,  $G$ , and  $A$  are the parameter value of each individual source, and the Greek letters represent the parameter weights for each respective principal component.

## 5 CONCLUSION

We studied a sample of 357 QSOs with optical brightness  $g < 17$ , which were produced by matching VLASS detections to the *Gaia* DR2 catalog and removing radio-bright stars by filtering out sources with significant proper motion. Our goal was to describe the characteristics of the host galaxy of each of our sources in order to determine if quasars are triggered due to external gravitational interactions.

Our study contained two main parts: First, we visually inspected and categorized each source by galaxy type and by presence of close companions or mergers using optical images taken from the PanSTARRs survey or the LSST, and by presence of extended radio emission using VLASS images. Second, we defined and measured three different quantitative parameters to objectively characterize our host galaxies, that described rotational asymmetry ( $A$ ), lumpiness/smoothness of the galaxy ( $G$ ), and brightness distribution of light in our galaxy ( $M_{20}$ ). From our results, we found that more than three-quarters of our sources in our sample are hosted by elliptical galaxies, and that sources at higher luminosity strongly tended to be elliptical in nature. Curiously, tidal tails galaxies, which are the most indicative of potential gravitational interaction, appear to be rather constrained in luminosity value. Tidal tails are most constrained within radio luminosity  $10^{22}$  to  $10^{24}$  W/Hz, and in optical luminosity  $10^{22}$  to  $10^{23}$  W/Hz. Almost all tidal tails can be found between luminosity ratios of 1 and 10. While this finding does not immediately reveal an answer to a quasar's genesis, it is noteworthy that the majority of these potential gravitational interactions occur in sources that have similar amounts of optical and radio radiation and this may be a hint of a potential correlation between luminosity ratio and galaxy structure.

Both individual analysis of each of our parameters plotted against luminosity and a collective Principal Component Analysis revealed that the most significant relationship between host galaxy structure and luminosity intensity is an inverse relationship between the Gini Coefficient of a source and its luminosity. This inverse relationship gives a crude power law of  $R_L = 10^{-4.04}G$  and  $O_L = 10^{-4.04}G$ , where  $R_L$  and  $O_L$  represent Radio Luminosity and Optical Luminosity, respectively. It is still significant that the most powerful QSO sources are those that appear to be hosted by the smoothest galaxies, those hosts that have fewer point sources or peaks of light that may represent clumps of material or activity whose gravity could influence the larger structure of the galaxy. While the answer to our question is still inconclusive, this new evidence does not inherently support the theory that external gravitational interactions are what trigger the QSO phenomena. For future work, we hope to compare our quantitative and qualitative sample of known quasars with quiescent galaxies, to see how substantially some of our visual classification and quantitative parameter analysis would change. Additionally, it would be beneficial to add more parameters to our quantitative analysis, such as the concentration (which is a ratio of division of  $r_{80}$  over  $r_{20}$ , where  $r_{20}$  and  $r_{80}$  are the radii where the galaxy contains 20% and 80% of its light, respectively) and the ellipticity (ratio of major to minor axis for each host galaxy). Additionally, instead of removing the quasar light from our source by using an annulus mask, we could instead do a PSF subtraction using a nearby star on our images in order to calculate the sersic index of our sources.

**REFERENCES**

- Chambers K. C., et al., 2016, arXiv e-prints, p. [arXiv:1612.05560](#)  
 Conselice C. J., Chapman S. C., Windhorst R. A., 2003, [ApJ](#), **596**, L5  
 Dey A., et al., 2019, [AJ](#), **157**, 168  
 Dunlop J. S., McLure R. J., Kukula M. J., Baum S. A., O'Dea C. P., Hughes  
     D. H., 2003, [MNRAS](#), **340**, 1095  
 Kuźmicz A., Jamrozy M., Bronarska K., Janda-Boczar K., Saikia D. J.,  
     2018, [ApJS](#), **238**, 9  
 Lacy M., et al., 2020, [PASP](#), **132**, 035001  
 Letawe Y., Letawe G., Magain P., 2010, [MNRAS](#), **403**, 2088  
 Lotz J. M., Primack J., Madau P., 2004, [AJ](#), **128**, 163  
 Scarlata C., et al., 2007, [ApJS](#), **172**, 406  
 Schmitt H. R., Antonucci R. R. J., Ulvestad J. S., Kinney A. L., Clarke C. J.,  
     Pringle J. E., 2001, [ApJ](#), **555**, 663